



Self-template synthesis of double-shell $\text{TiO}_2@\text{ZIF}-8$ hollow nanospheres via sonocrystallization with enhanced photocatalytic activities in hydrogen generation



Ming Zhang^a, Qigao Shang^a, Yuqi Wan^a, Qingrong Cheng^{a,*}, Guiying Liao^b, Zhiqian Pan^a

^a Key Laboratory for Green Chemical Process of Ministry of Education, Wuhan Institute of Technology, Wuhan 430073, PR China

^b Engineering Research Center of Nano-Geo Materials of Ministry of Education, China University of Geosciences, Wuhan 430074, PR China

ARTICLE INFO

Keywords:

Hybrid photocatalyst
Hollow TiO_2 nanospheres
 $\text{ZIF}-8$
Hydrogen evolution
 $\text{TiO}_2@\text{ZIF}-8$ nanocomposites

ABSTRACT

The photocatalytic hydrogen evolution on inorganic semiconductors has been studied for several decades. However, the conversion efficiency of solar energy is still poor caused by the recombination of photo-generated electron-hole pairs. Semiconductors - metal organic frameworks (MOFs) hybrid photocatalysts are being regarded as promising candidates due to large surface area and porosity. Here we reported the coordinative integration of a composite material with efficient capacity of H_2 evolution driven by solar light, namely $\text{TiO}_2@\text{ZIF}-8$, made up of titanium dioxide hollow nanospheres (TiO_2 HNPs) externally decorated with zeolitic imidazolate framework-8 (ZIF-8) via a facile sonochemical route. The resulting composite demonstrates the high dispersion of ZIF-8 on the surface of TiO_2 HNPs and this kind of close connection makes for an efficient photocatalyst through the synergistic effect. Up to 50.89% of apparent quantum efficiency (AQE), the hybrid double-shell HNPs exhibits 3.5 times higher H_2 evolution rate (HER) than the bare TiO_2 HNPs under solar light and shows good stability and recyclability. It is further proposed by photoluminescence spectra and optoelectronic measurement that the remarkably enhanced photocatalytic activity of $\text{TiO}_2@\text{ZIF}-8$ is not only attributed to the efficient charge separation with electron injection from ZIF-8 to TiO_2 HNPs, but also more active reaction sites provided by cavity structure of ZIF-8. Overall, this work exemplifies that surface engineering of semiconductors with MOFs is a great strategy to achieve advanced photocatalytic performance for solar energy conversion.

1. Introduction

Along with the rapid development of economy and globalization, demand of energy source increases continually. As a green and renewable energy, the solar energy is abundant, economic and non-pollution. Photocatalysis is an environmental and promising technology to convert solar energy into chemical energy including water splitting [1,2], solar cells [3,4], hydrogen generation [5,6] and carbon dioxide conversion [7,8]. One of the most attractive options is the conversion of solar energy into H_2 through a water splitting process with the help of semiconductor-based photocatalysts [9–11].

Since the pioneering research of water splitting by Fujishima and Honda on TiO_2 electrode [12], more and more inorganic semi-conductive materials such as ZnO , WO_3 , CdS and ZnS , have been studied in global energy and environmental issues [13–19]. These metal oxide semiconductive nanomaterials have attracted many attentions due to the advantages of nontoxicity, thermal and chemical stability.

However, the low surface area and adsorption ability of TiO_2 limit the photocatalytic H_2 evolution rate (HER). Therefore, large amounts of works have been carried out to increase the specific surface area by changing the morphologies of TiO_2 (nanofibers, hierarchical spheres and hollow nanoparticles) [20–22]. In addition, the higher solar to chemical energy conversion of TiO_2 could be realized by extending light absorption region and by enhancing the charge separation efficiency, the most common form of which are doping modification and heterojunction fabrication [18,23–27].

Metal organic frameworks (MOFs) have attracted increasing research interest for their potential value as adsorbents and catalysts due to high surface area, large pore size, tunable, well-defined nanometer-scale cavities and chemical tailorability [28]. Generally, the bridge ligand of MOFs can serve as antenna to harvest energy under light, followed by the charge transfer from organic linker to metal-connecting node (LMCT, ligand-to-metal charge transfer) [29,30], or just metal cluster can be directly photoexcited [31,32]. However, the

* Corresponding author.

E-mail address: chengqr383121@sina.com (Q. Cheng).

photoactivity could not reach the quality as high as traditional semiconductors due to low charge separation efficiency. In this regard, some pre/post-synthesis modifications have been studied to improve the chemical stability and extend light adsorption region [33,34]. On the other hand, MOFs combining with other photocatalysts to form semiconductor-MOF hybrid structures can boost the photocatalytic efficiency. Different with the single-component photocatalyst readily suffering from rapid electron-hole recombination, some unique physical and chemical properties of both MOFs and semiconductors have been combined to get an improvement in photocatalytic efficiency during coupling [35]. To date, several TiO_2 -MOF hybrid photocatalysts have been synthesized, such as $\text{TiO}_2/\text{PCN}-222(\text{Zn})$ [36], Co-ZIF-9/ TiO_2 [37], $\text{TiO}_2/\text{NH}_2\text{-UiO}-66$ [38], $\text{TiO}_2@/\text{MIL}-101$ [39], and have showed higher potential photocatalytic activity as compared to single catalyst. As a typical MOF, ZIF-8, constructed by Zn(II) and 2-methylimidazole ligands, with high specific surface area, regular pores and excellent water stability, has been widely used as catalyst in some reactions including Friedel-Crafts acylation [40], Knoevenagel reaction [41] and photocatalytic reaction [42]. Recently, some semiconductor/ZIF-8 hybrid photocatalysts also have been studied, for example, the molecule size selective and good photocatalytic activity from $\text{ZnO}@\text{ZIF}-8$ [43,44]; enhancement in photocatalytic conversion of CO_2 into liquid CH_3OH fuel from ZIF-8/ Zn_2GeO_4 [45]; higher efficiency in Rhodamine B photodegradation from $\text{TiO}_2/\text{ZIF}-8$ [46]. In spite of some studies on these kind of hybrid composites $\text{TiO}_2@/\text{MOFs}$, there are few researches in H_2 generation involving $\text{TiO}_2@/\text{ZIF}-8$. Moreover, reports on enhancing the photocatalytic H_2 evolution of TiO_2 by coupling with ZIF-8 remain limited. Meanwhile, as part of our ongoing studies on the photocatalyst, that how to improve the surface area and provide the transfer pathway for separation of electrons and holes for photocatalytic activity enhancement, is where we are further interested in.

In this work, we designed and synthesized double-shell $\text{TiO}_2@/\text{ZIF}-8$ hollow nanospheres via sonocrystallization. Our strategy includes two aspects: one is the topography optimization of TiO_2 with higher surface area, the other is the hybrid combination with ZIF-8 for enhancing photocatalytic efficiency. The general stepwise strategy for the double-shell $\text{TiO}_2@/\text{ZIF}-8$ hollow nanospheres is presented in Fig. 1. As expected, sonocrystallization as an effective and rapid process to generate new nanostructure materials [47], makes growth of ZIF-8 on the surface of these hollow spheres to yield $\text{TiO}_2@/\text{ZIF}-8$ hybrid composite. In addition, the charging sequence is proved to be an important factor that influences the coverage in synthesis. To provide a further investigation of the mechanism of photocatalytic H_2 evolution in this field, several analytical and spectroscopic techniques were used. The HER of prepared nanocomposite was proven significantly higher than two single components. This was attributed primarily to efficient charge separation with electron injection from ZIF-8 to TiO_2 HNPs, and more active sites supplied by ZIF-8 on the surface of hollow sphere.

2. Experimental

2.1. Synthesis of polystyrene nanospheres

Polystyrene (PS) nanospheres were used as the template. Instead of conventional synthesis with longer hours, a new microwave synthesis method was applied to preparation of PS for improving the efficiency and productivity. In brief, 0.050 g of sodium dodecyl sulfate (SDS emulsifier) and 15 g of styrene monomer were added to 80 mL water with stirring in a three-necked flask. One end of flask was connected into a nitrogen cylinder and the other end was connected into water. A return line was upright connected with middle neck of flask. After removing air totally, the temperature was raised to 80 °C by microwave reactor under N_2 . Then, 20 mL of an aqueous solution containing 0.15 g of potassium persulfate as initiator was added dropwise from return line into microwave reactor. The mixture was stirred for another 90 min in the microwave system, and the PS nanospheres were precipitated by addition of 10 g of sodium chloride. The final product was washed three times with deionized water and dried in a vacuum oven at 60 °C.

2.2. Synthesis of TiO_2 hollow nanospheres (TiO_2 HNPs) and their carboxylation

A mixed solvent ethanol/acetonitrile (3:1, v/v) was dried over molecular sieve for 24 h. Then, 0.50 mL of tetrabutyl titanate was added to 20 mL of mixed solvent and stirred for 10 min in a sealed environment. 0.017 g of PS nanospheres was added to 90 mL of mixed solvent in another flask, and the suspension was sonicated to disperse the particles. Then, 0.30 mL of 28% ammonia solution, 0.06 mL of deionized water, and 20 mL of mixed solvent containing tetrabutyl titanate were added dropwise to the PS suspension in succession. Next, the mixture was stirred for 2 h before centrifuging and being washed three times with ethanol. The resulting powder was dried in a vacuum oven at 60 °C. The PS@ TiO_2 core-shell particles were then annealed in air at 500 °C at a heating rate of 3 °C/min to get the TiO_2 HNPs;

0.45 g of succinic anhydride was dissolved in 30 mL DMF, and 1.0 mL of (3-aminopropyl) triethoxysilane was added gradually. After the mixture was stirred for 3 h at room temperature, 2 mL deionized water and 10 mL of DMF solvent containing 0.50 g of TiO_2 HNPs. After being stirred for 8 h, the final carboxylates of TiO_2 HNPs was washed three times with ethanol and dried in a vacuum oven at 60 °C.

2.3. Synthesis of double-shell $\text{TiO}_2@/\text{ZIF}-8$ hollow nanospheres

0.08 g of TiO_2 HNPs carboxylation and 0.11 g of 2-methylimidazole were dispersed in 20 mL of methanol under ultrasonic treatment. Then, 10 mL of methanol solvent containing 0.19 g of $\text{Zn}(\text{NO}_3)_2 \cdot 6\text{H}_2\text{O}$ was added dropwise into the system under ultrasonic. The ultrasonic treatment was carried out at a power level of 200 W and kept working for 15 min. Then, the participate was collected by centrifugation and washed three times with methanol. The resulting $\gamma\text{-TiO}_2@/\text{ZIF}-8$ powder was dried in a vacuum oven at 60 °C.

Two another $\text{TiO}_2@/\text{ZIF}-8$ samples named α -/β- $\text{TiO}_2@/\text{ZIF}-8$ were

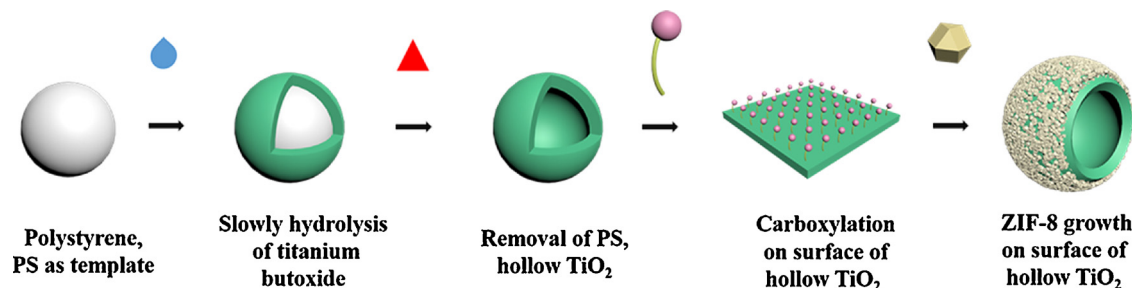


Fig. 1. Schematic illustration of the integration of double-shell $\text{TiO}_2@/\text{ZIF}-8$ hollow nanosphere.

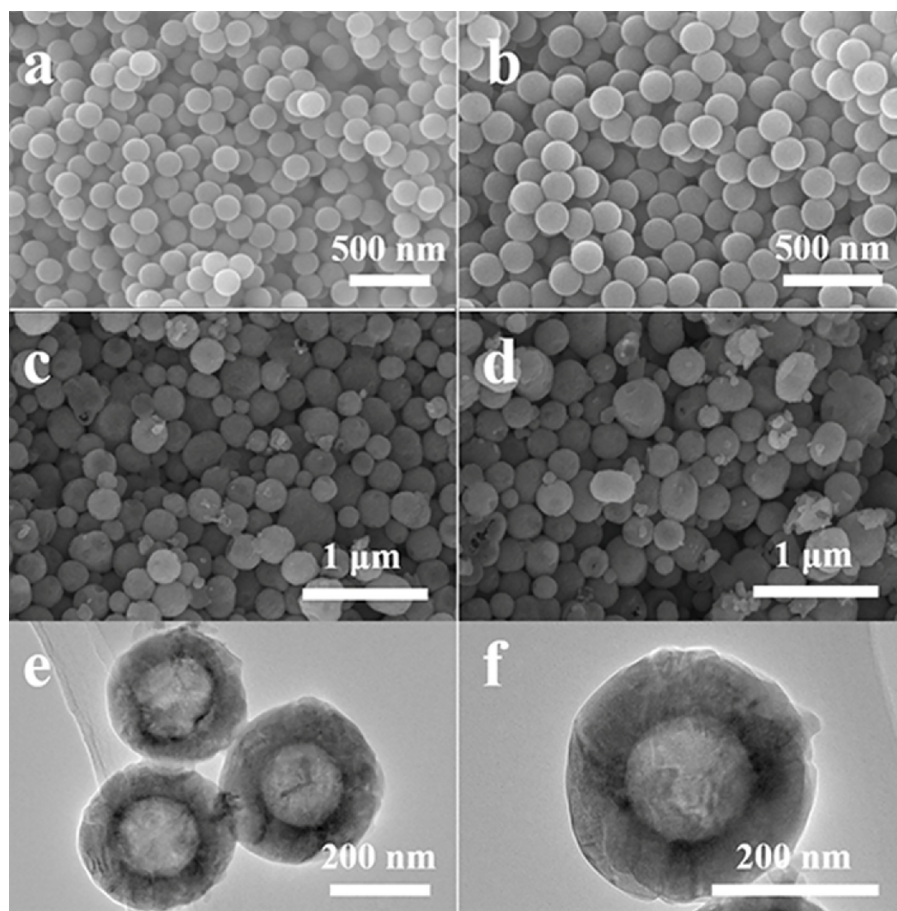


Fig. 2. SEM images of polystyrene spheres (a and b), SEM images (c and d) and TEM images (e and f) of TiO_2 HNPs.

synthesized with different charging sequence from conventional method or sonocrystallization: (α). 0.08 g of TiO_2 HNPs carboxylation was dispersed in 10 mL of methanol, and 10 mL of methanol solution of $\text{Zn}(\text{NO}_3)_2 \cdot 6\text{H}_2\text{O}$ (0.60 g) was added. After the solution was stirred for 15 min at room temperature, 10 mL of methanol solution of 2-methylimidazole (0.33 g) was added, and the mixture was stirred for a further 5 h; (β) 0.19 g of $\text{Zn}(\text{NO}_3)_2 \cdot 6\text{H}_2\text{O}$ was dissolved om 10 mL of methanol and begin the ultrasonic treatment. Then, 10 mL of methanol suspension of TiO_2 HNPs carboxylation (0.08 g) and 10 mL of methanol solution of 2-methylimidazole (0.11 g) were both added dropwise to the ultrasonic system synchronously at a same rate for about 15 min. And the ultrasonic treatment was carried out at a power level of 200 W and keep working for another 15 min. The resulting α -/ β - TiO_2 @ZIF-8 powder were collected in the same way of γ - TiO_2 @ZIF-8.

2.4. Characterization

Powder X-ray diffraction (XRD) was carried out on a Bruker D8 Advance X-ray diffractometer operated at 40 kV and 40 mA using $\text{Cu K}\alpha$ radiation ($\lambda = 0.15418 \text{ nm}$). Fourier transform infrared spectroscopy (FTIR) was performed on a Nicolet 6700 FTIR Spectrometric Analyzer using KBr pellets. Raman measurement was carried out using a RINT 2000 Raman spectroscopy. The size and morphology of the samples were observed with a scanning electron microscope (SEM, Hitachi-S-4800) at 5 kV. The transmission electron microscopy (TEM) images were obtained using a JEOL JEM-2100 F electron microscope operated at 200 kV. The elemental composition of the samples was observed by energy dispersive X-ray spectroscopy (EDX) coupled to TEM. X-ray photoelectron spectroscopy was carried out on Thermo ESCALAB 250XI using monochromatized $\text{Al K}\alpha$ at $h\nu = 1486.6 \text{ eV}$. The binding energies

were calibrated to the C1s peak by 284.6 eV. The Brunauer-Emmett-Teller (BET) surface areas were recorded by ASAP 2020 V4.00 with nitrogen absorption at 77 K. Thermal gravimetric (TG) measurement was taken on a thermal instrument (Netzsch STA 449 F1) with a heating rate of 10 °C/min. UV-vis diffuse reflectance spectra (DRS) of the samples were recorded on a UV-vis spectrophotometer (Hitachi U-4100) within a wavelength range of 200–800 nm, and BaSO_4 was used as the reflectance standard. The low temperature electronic paramagnetic resonance (EPR) spectra was recorded at 77 K on Bruker A300 electron spin resonance spectrometer. Photoluminescence (PL) spectra was detected with a Hitachi F4600 fluorescence spectrophotometer. The time-resolved photoluminescence was conducted with a Horiba FLTCSPC fluorescence spectrophotometer. Transient photocurrent density and electrochemical impedance spectra (EIS) were analyzed on an electrochemical workstation (Corrtest CS350) in a standard three-electrode system and the related details about these experiments were recorded in Supplementary data.

2.5. Photocatalytic hydrogen evolution process

Photocatalytic reactions of H_2 evolution were carried out in a closed gas circulation system with an external-irradiation Pyrex-cell. The light source was a 300 W xenon lamp. Typically, 100 mg of photocatalyst was first ultrasonically dispersed in 270 mL of methanol solution (20 vol%). Before light irradiation, the reactor was sealed to a gastight condition with high vacuum grease and purged by a vacuum pump to remove the residual air. Then, magnetic stirring was used to stabilize the suspension during the whole photocatalytic H_2 evolution. The amounts of generated H_2 was analyzed by an online gas chromatograph equipped with a thermal conductivity detector. The intensity of the

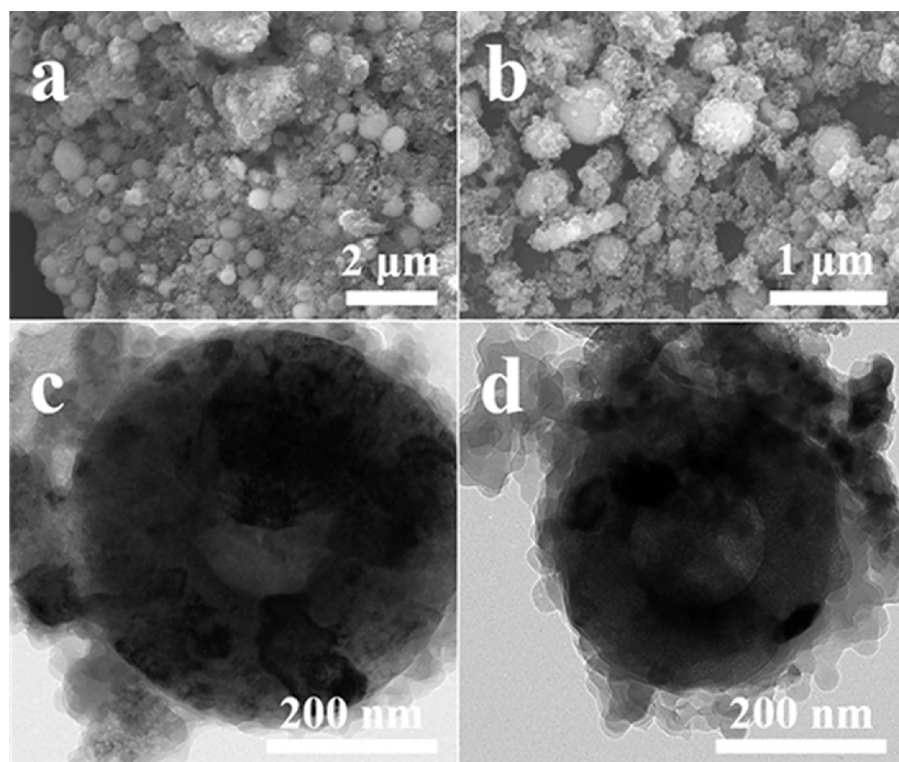


Fig. 3. SEM images (a and b) and TEM images (c and d) of γ -TiO₂@ZIF-8.

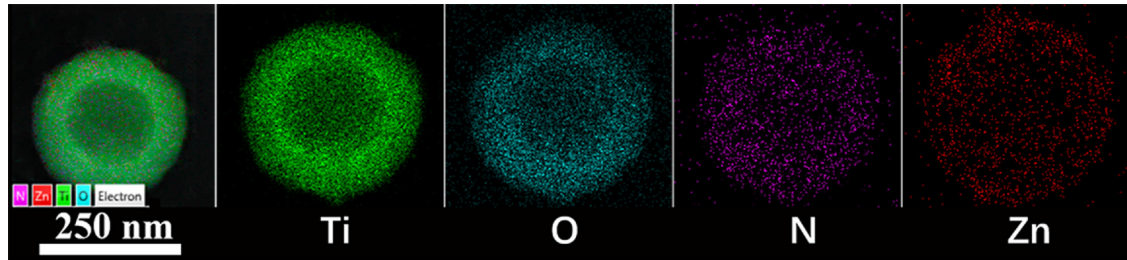


Fig. 4. STEM image, Ti, O, N and Zn STEM EDX mapping of γ -TiO₂@ZIF-8.

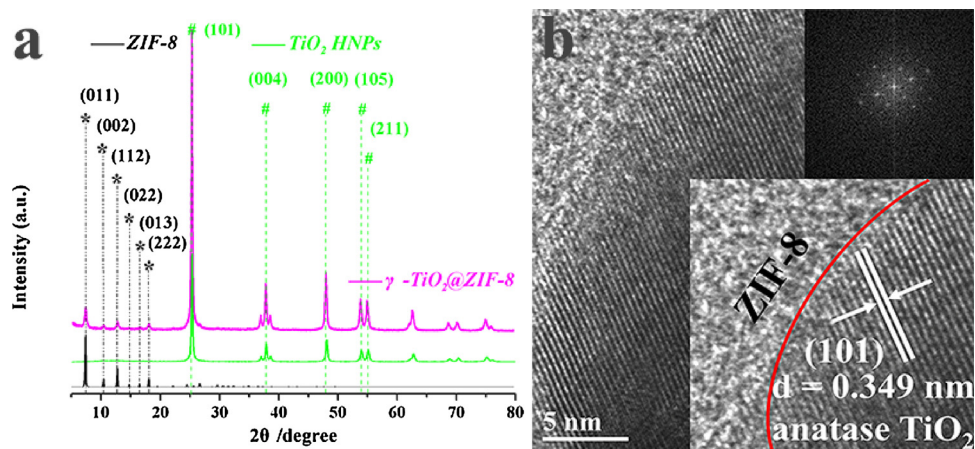


Fig. 5. (a) PXRD patterns of ZIF-8, TiO₂ HNPs and γ -TiO₂@ZIF-8; (b) HRTEM image and FFT image (inserted) of γ -TiO₂@ZIF-8.

light at 380–800 nm was measured to be 1.5 mW/cm² with a 380 nm (± 5 nm) band-pass filter. And the apparent quantum efficiency (AQE) of photocatalyst was calculated using Eq. (1) according to previously reported work [48,49]. The detailed information for AQE test and calculation were shown in Supplementary data.

$$\text{AQE} = \frac{\text{number of reacted electrons}}{\text{number of incident photons}} \times 100\% \quad (1)$$

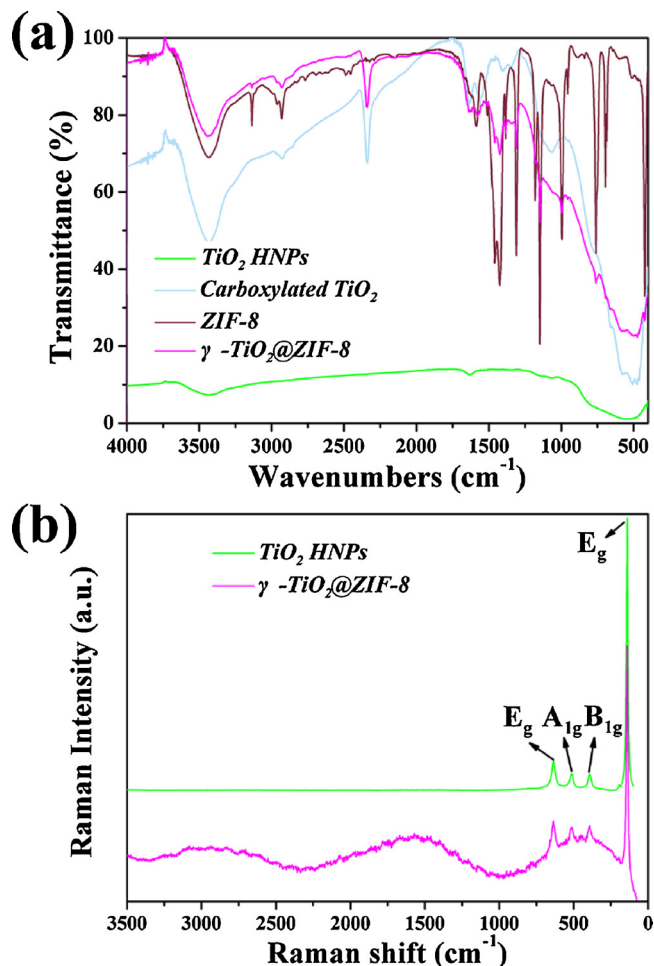


Fig. 6. (a) FTIR spectra of TiO_2 HNPs, carboxyl- TiO_2 , ZIF-8 and $\gamma\text{-TiO}_2@\text{ZIF-8}$; (b) Raman pattern of TiO_2 HNPs and $\gamma\text{-TiO}_2@\text{ZIF-8}$.

3. Results and discussion

As the template in preparation of TiO_2 hollow nanospheres (TiO_2 HNPs), the morphology of polystyrene (PS) is spherical with a uniform size, whose diameter is about 160 nm, shown in SEM images (Fig. 2a,b). Since PS@ TiO_2 core-shell particles were annealed to remove the template, TiO_2 HNPs were obtained. SEM images (Fig. 2c,d) indicated that the morphology of TiO_2 particle is spherical just seen from the outside. However, it is hollow inside with a thickness of 60 nm shown in TEM images (Fig. 2e,f).

As shown in SEM images (Fig. 3a,b), the size of ZIF-8 in $\gamma\text{-TiO}_2@\text{ZIF-8}$ was smaller than that of traditional ZIF-8 from reported work. It showed that the process of sonocrystallization can inhibit the self-nucleus growth of ZIF-8. The growth of ZIF-8 tended to occur along with the surface of TiO_2 HNPs carboxylation. By contrast, over-independence of two components of $\alpha/\beta\text{-TiO}_2@\text{ZIF-8}$ existed in synthesis of the hybrid material, and these defects, such as the similarity in size, some failures in coverage on the surface of TiO_2 HNPs, can be seen from SEM/TEM images in Figure S1. From TEM images of $\gamma\text{-TiO}_2@\text{ZIF-8}$ (Fig. 3c,d), in addition, it reflected that the sonocrystallization did not destroy the hollow morphology of TiO_2 , and that the process restricted the speed and size of ZIF-8 in growth which is helpful for the coverage.

Moreover, high-angle annular dark-field scanning transmission electron microscopy (HAADF-STEM) and STEM EDX mappings were performed to further confirm the composition of the $\gamma\text{-TiO}_2@\text{ZIF-8}$. Fig. 4 displayed the distribution of elements in the $\gamma\text{-TiO}_2@\text{ZIF-8}$ hybrid. The green, cyan, purple and red colors represented the distributions of Ti, O, N and Zn, respectively. The distributions of four elements

showed a regular sphere. Among these elements, Ti and O, mostly from TiO_2 , evenly distributed across the shell of TiO_2 HNPs, and the sphere-inner density is too much lower than the outer. While N and Zn, originated from ZIF-8, evenly distributed across the whole surface of TiO_2 HNPs, and there is no difference in density between the inner and outer sections. The diameters of distribution in N and Zn images, larger than in Ti and O images, can further confirm the presence of the MOF layer.

The crystalline structure of prepared samples was further confirmed by the characteristic PXRD diffraction analysis. As shown in Fig. 5a, the distinct peaks (signed as *) at 7.41° , 10.48° , 12.81° , 14.78° , 16.53° and 18.13° were ascribed to the (011), (002), (112), (022), (013) and (222) reflections of ZIF-8, which are consistent with previously reported results, as well as with the simulated one (Fig. S2) [50,51]. And the diffraction peaks (signed as #) at 25.36° , 37.89° , 48.12° , 53.94° and 55.09° were corresponding to the (101), (004), (200), (105) and (211) planes of TiO_2 , which can be indexed to the anatase TiO_2 (JCPDS No. 21-1272). The lattice fringe with d-spacing of 0.349 nm in the high resolution TEM (HRTEM) image and the Fast Fourier Transform (FFT) image (Fig. 5b) further confirmed the anatase TiO_2 . As for $\gamma\text{-TiO}_2@\text{ZIF-8}$ composite, the patterns obviously consist of all the diffraction peaks of ZIF-8 and TiO_2 . Additionally, no other apparent diffraction peaks and no shifts in the peak positions for $\gamma\text{-TiO}_2@\text{ZIF-8}$ can be observed, suggesting that the phase composition and crystallinity of TiO_2 did not change after the synthesis process applied for the ZIF-8 nucleation and growth. Hence, the PXRD provided direct evidence that both TiO_2 and ZIF-8 structures were present and not altered by the synthesis process applied for the development of the double-shell $\text{TiO}_2@\text{ZIF-8}$ hollow nanospheres.

The FTIR spectroscopy enable to get a greater insight into the interactions between the two composite components (Fig. 6a). It can be observed that the as-prepared $\gamma\text{-TiO}_2@\text{ZIF-8}$ showed vibration bands at 422 cm^{-1} (Zn–N stretch), 1578 cm^{-1} (C=N stretch), 1421 cm^{-1} and 997 cm^{-1} (C–N stretch), 1147 cm^{-1} and 1308 cm^{-1} (imidazole bending) which were typically characteristic for ZIF-8 [52,53]. The vibration band around 488 cm^{-1} was the typical vibration of Ti–O–Ti bond in TiO_2 . It is worth noting that the appearance of characteristic COO- M^+ band at 1311 cm^{-1} demonstrated the successful carboxyl group modification in TiO_2 HNPs, as well as ZIF-8-coating in TiO_2 HNPs [39]. Moreover, another new adsorption band at 514 cm^{-1} can be attributed to the formation of typical N-Ti-O bond [46]. The Raman spectroscopy of TiO_2 HNPs and $\gamma\text{-TiO}_2@\text{ZIF-8}$ were shown in Fig. 6b, The Raman active fundamental modes corresponding to 140 cm^{-1} (E_g), 392 cm^{-1} (B_{1g}), 513 cm^{-1} (A_{1g}), 635 cm^{-1} (E_g) matched with the anatase structure of TiO_2 in TiO_2 HNPs [54]. The E_g mode (141 cm^{-1} and 637 cm^{-1}) for $\gamma\text{-TiO}_2@\text{ZIF-8}$ composite was slightly blue-shifted compared with TiO_2 HNPs and its intensity was lower. It was referred to the shrink of the grain size and decrease of the oxygen vacancy concentration during the sonocrystallization [55,56]. To verify this, the low temperature EPR experiment was carried out. It was reported that the surface Ti^{3+} would tend to adsorb atmospheric O_2 , and reduce the O_2 into O_2^- , leaving the oxygen vacancy, which shows an EPR signal at $g = 2.00$ [57]. As shown in Fig. 3S, the intensity of signal appeared in $\gamma\text{-TiO}_2@\text{ZIF-8}$ at $g = 2.00087$ was much weaker than in bare TiO_2 HNPs, indicating that less oxygen vacancies existed on the surface of $\gamma\text{-TiO}_2@\text{ZIF-8}$, which was corresponding to the Raman shift change.

X-ray photoelectron spectroscopy (XPS) was employed to investigate the chemical state and the composition of the outermost surface. The survey spectra (Fig. 7a) confirmed the presence of Ti, Zn, C, O and N elements in $\text{TiO}_2@\text{ZIF-8}$. In the Ti 2p XPS spectra (Fig. 7b), the two peaks at 458.3 eV and 464.2 eV are assigned to $\text{Ti} 2p_{3/2}$ and $\text{Ti} 2p_{1/2}$, respectively, corresponding to Ti^{4+} in TiO_2 [58,59], while two other peaks at 457.0 eV and 463.0 eV can be attributed to the $\text{Ti} 2p_{3/2}$ and $\text{Ti} 2p_{1/2}$, which is a characteristic of Ti species in lower oxidation state (Ti^{3+}) [60]. In Fig. 7c, the binding energies of 1021.7 eV and 1044.9 eV for Zn 2p are attributed to Zn $2p_{3/2}$ and Zn $2p_{1/2}$, respectively [61]. In the C 1s spectra (Fig. 7d), the binding energies of

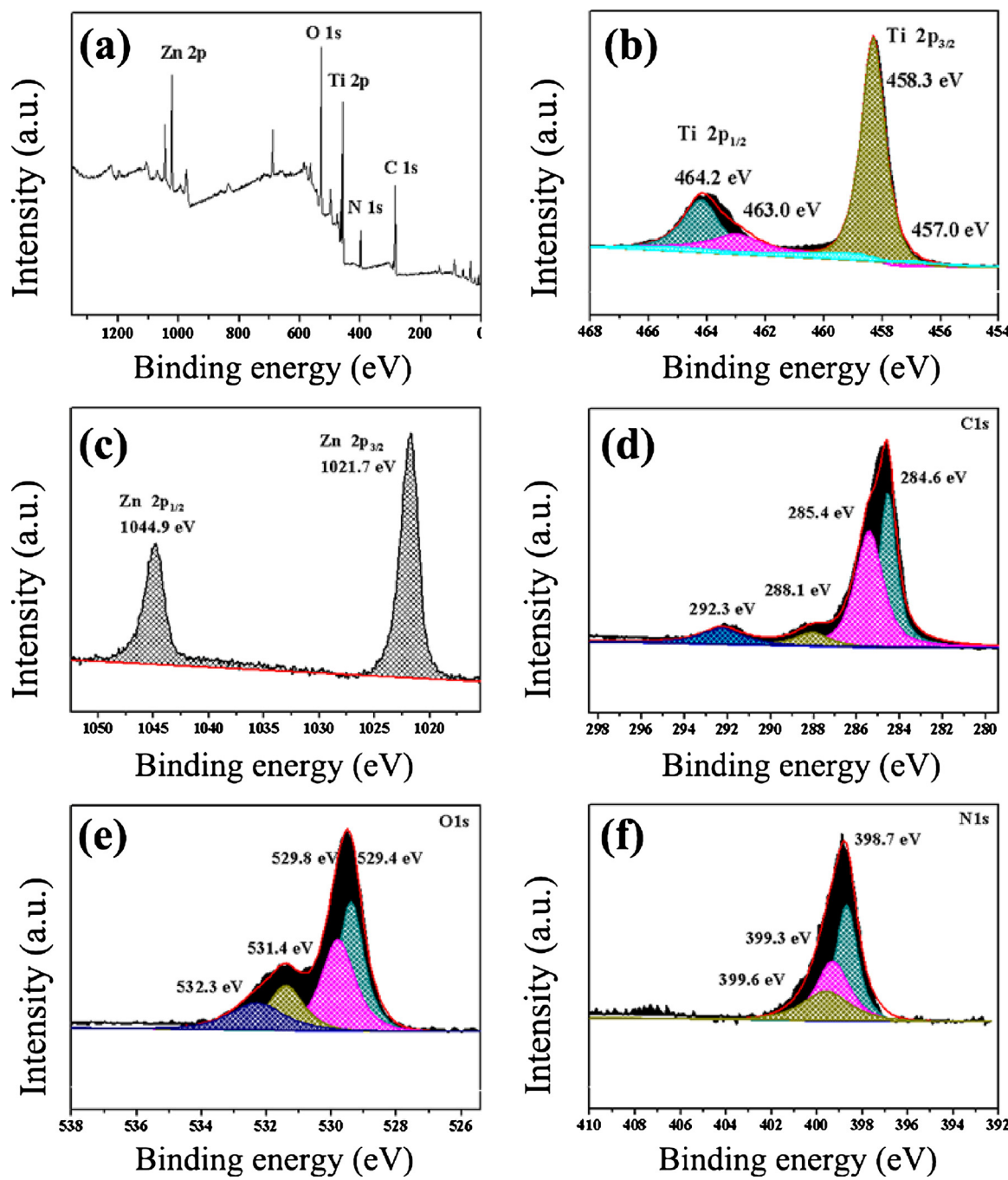


Fig. 7. (a) XPS survey spectrum of γ -TiO₂@ZIF-8; (b–f) Ti 2p, Zn 2p, C 1s, O 1s, N 1s XPS spectrum of γ -TiO₂@ZIF-8.

284.6 eV, 285.4 eV, 288.1 eV and 292.3 eV can be assigned to the C–C, C–N, –COOH and π –C bonds, respectively, indicating the successful carboxylation on TiO₂ HNPs [62–64]. As shown in Fig. 7e, the O 1s region can be fitted into four peaks at 529.4 eV, 529.8 eV, 531.4 eV and 532.3 eV. The peaks at 529.8 eV, 531.4 eV and 532.3 eV belonged to the O–Ti bond in TiO₂ HNPs, O–Si bond from (3-aminopropyl) triethoxysilane and O–H bond [64,65]. An additional peak of 529.4 eV can be assigned to the formed O–Zn bond by the coordination between carbonate O atoms and Zn²⁺, confirming the interaction between TiO₂ HNPs and ZIF-8 [61,66]. Moreover, three N 1s peaks of 398.7 eV, 399.3 eV and 399.6 eV (Fig. 7f) were attributed to N–C bond from imidazole ring in ZIF-8, –NH– bond and N–Ti–O bond [45,63,66]. The chemical N–Ti–O linkage indicated that part of O atoms in the surface of TiO₂ HNPs were replaced by N atoms from imidazole ring,

which further confirmed the successful ZIF-8 loading on TiO₂ HNPs. Hence, the XPS measurements proved that the as-prepared hybrid product is composed of TiO₂ and ZIF-8.

The thermal stability of prepared samples was evaluated by thermal gravimetric (TG) analysis. As shown in Fig. 8, for the bare TiO₂ HNPs, TG analysis showed no significant decomposition, and only 0.75% mass loss was observed up to 900 °C. For the carboxylates of TiO₂ HNPs, the TG curve exhibited a gradual mass-loss step of 7.08% up to 900 °C starting with 450 °C, which can be attributed to the decomposition of organic ingredients of (3-aminopropyl) triethoxysilane and succinic anhydride on the surface of TiO₂ HNPs via coupling action. For the bare ZIF-8, there was no obvious mass loss up to 500 °C, and a mass-loss step of 40.29% occurred, corresponding to the collapse of the ZIF-8 structure. For the γ -TiO₂@ZIF-8, a total mass loss of 17.84% in the measured

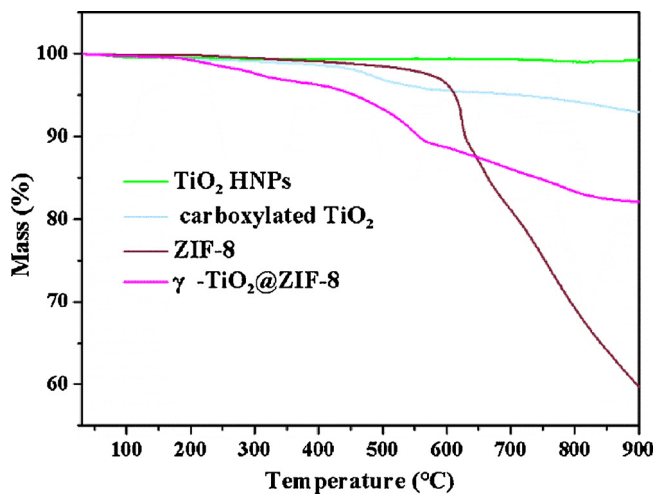


Fig. 8. TG curves of TiO₂ HNPs, carboxyl-TiO₂, ZIF-8 and γ -TiO₂@ZIF-8.

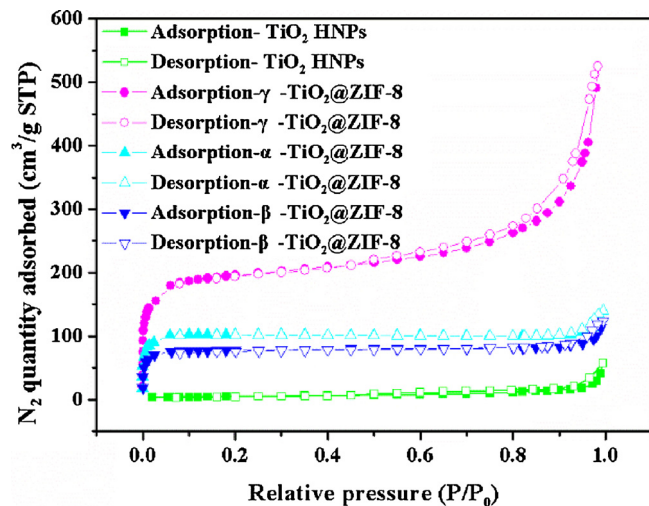


Fig. 9. N₂ absorption isotherms of TiO₂ HNPs and α -/ β -/ γ -TiO₂@ZIF-8.

Table 1
Physical properties of composites.

Materials	S _{BET} (m ² /g)	Pore volume (cm ³ /g)	Average diameter of meso/microporous (nm)
TiO ₂ HNPs	17	0.09	3.5
α	343	0.22	31
β	260	0.19	2.6
γ	668	0.81	3.9
ZIF-8	1123	0.62	1.2

temperature range means that the sample contained around 27% of ZIF-8 and 73% of TiO₂. In addition, it was also revealed that the stable existence of ZIF-8 shell in the hybrid product from decomposition occurring just at high temperature.

The permanent porosity of prepared samples was estimated by N₂ adsorption-desorption isotherms (Fig. 9). Table 1 summarized the BET surface area, pore volume and average pore diameter. As expected, the surface area of TiO₂ HNPs was found to be very low when compared to reported ZIF-8 [67]. The curves for TiO₂ HNPs are a type IV isotherm of a mesoporous material, which showed low adsorption at low pressures and multilayer adsorption at high pressures owing to slits caused by assembly of TiO₂ spheres. The specific BET surface area was 17 m²/g. For comparison, the BET surface areas of three kinds of TiO₂@ZIF-8 (α -/ β -/ γ -), which fit well with a type I isotherm, were higher than that

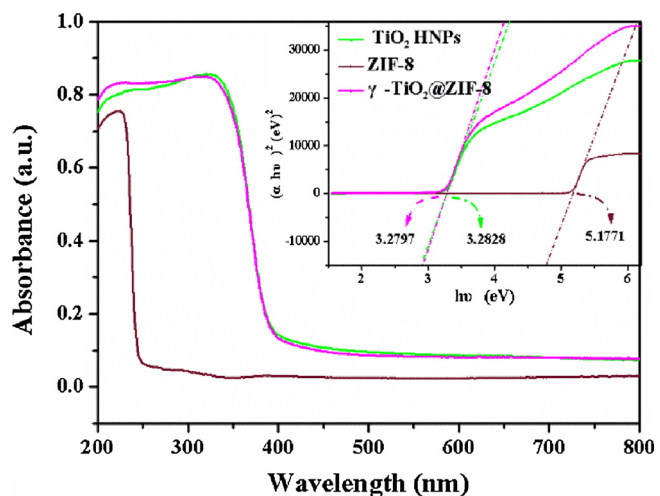


Fig. 10. UV-vis visible absorption spectra of TiO₂ HNPs, ZIF-8 and γ -TiO₂@ZIF-8; Fit curves of Tauc plot (inset one).

of bare TiO₂ HNPs due to the loading of microporous frameworks of ZIF-8. And the highest is γ -TiO₂@ZIF-8 of 667.9 m²/g. The diversity might be caused by different treatment and varied charging sequence in synthesis process. The smallest size of ZIF-8 in three TiO₂@ZIF-8 compositions was obtained from γ -TiO₂@ZIF-8 via sonocrystallization in a certain charging sequence. The result implied that γ -TiO₂@ZIF-8 can provide more active sites in photocatalytic reaction.

The optical property of prepared samples was investigated by UV-vis diffuse reflectance spectroscopy (DRS). As shown in Fig. 10, bare ZIF-8 owns an absorption edge around 230 nm. γ -TiO₂@ZIF-8 showed an absorption band in the region of 340–390 nm, similar with the absorption band of bare TiO₂ HNPs. The optical band gaps of the samples can be estimated using the Tauc plot, i.e., the curve of converted $(\alpha h\nu)^2$ versus $h\nu$ from the UV-vis spectrum, where α , ν , A, and E_g are the absorption coefficient, light frequency, proportionality constant and band gap, respectively. The plot of $(\alpha h\nu)^2$ versus the energy of the absorbed light would give the band gaps of the samples. The E_g value was determined by measuring the x-axis intercept of an extrapolated tangential line from the linear region of the curve. The band gaps of ZIF-8, TiO₂ HNPs, γ -TiO₂@ZIF-8 were estimated to be 5.18 eV, 3.28 eV and 3.28 eV respectively (inset one in Fig. 10). And the decrease of E_g values of the samples is helpful in enhancing the photocatalytic efficiency [68,69]. In addition, proper matching of the valence band E_v (vs. NHE) and conduction band E_c (vs. NHE) was also important for evaluating photocatalysis [70]. The E_v position of γ -TiO₂@ZIF-8 was determined by linear extrapolation of the leading edges of VB-XPS spectra to the baselines (Fig. S4). The E_v position of γ -TiO₂@ZIF-8 located at \sim 2.08 eV. Therefore, the E_c position (\sim -1.19 eV) was obtained from (E_v - E_g). Besides, the conduction band edges of bare TiO₂ and bare ZIF-8 were calculated to be -0.31 eV and -4.73 eV respectively, according to the empirical formula, namely E_c = X - E_e - 0.5E_g, where X is the constant of electronegativity (5.81 eV for TiO₂ and 2.36 eV for ZIF-8), E_e value is 4.50 eV [49].

The photocatalytic performance of prepared samples was evaluated with hydrogen evolution from water under artificial sunlight irradiation using methanol solution (20 vol %) as the sacrificial reagent. As shown in Fig. 11a, b, no H₂ evolution could be detected just in the presence of bare ZIF-8 due to its poor visible-light absorption capability. The bare TiO₂ HNPs showed a lower photocatalytic H₂ evolution rate (HER) of 74.6 μ mol g⁻¹ h⁻¹ compared with three TiO₂@ZIF-8 composites, attributing to its lower specific surface area and faster charge carrier recombination. Another physical mixture of TiO₂ HNPs and ZIF-8 also showed a lower rate of 4.63 μ mol g⁻¹ h⁻¹ (Fig. S5). Whereas the photocatalytic activity can be notably enhanced by the coverage of ZIF-8 in

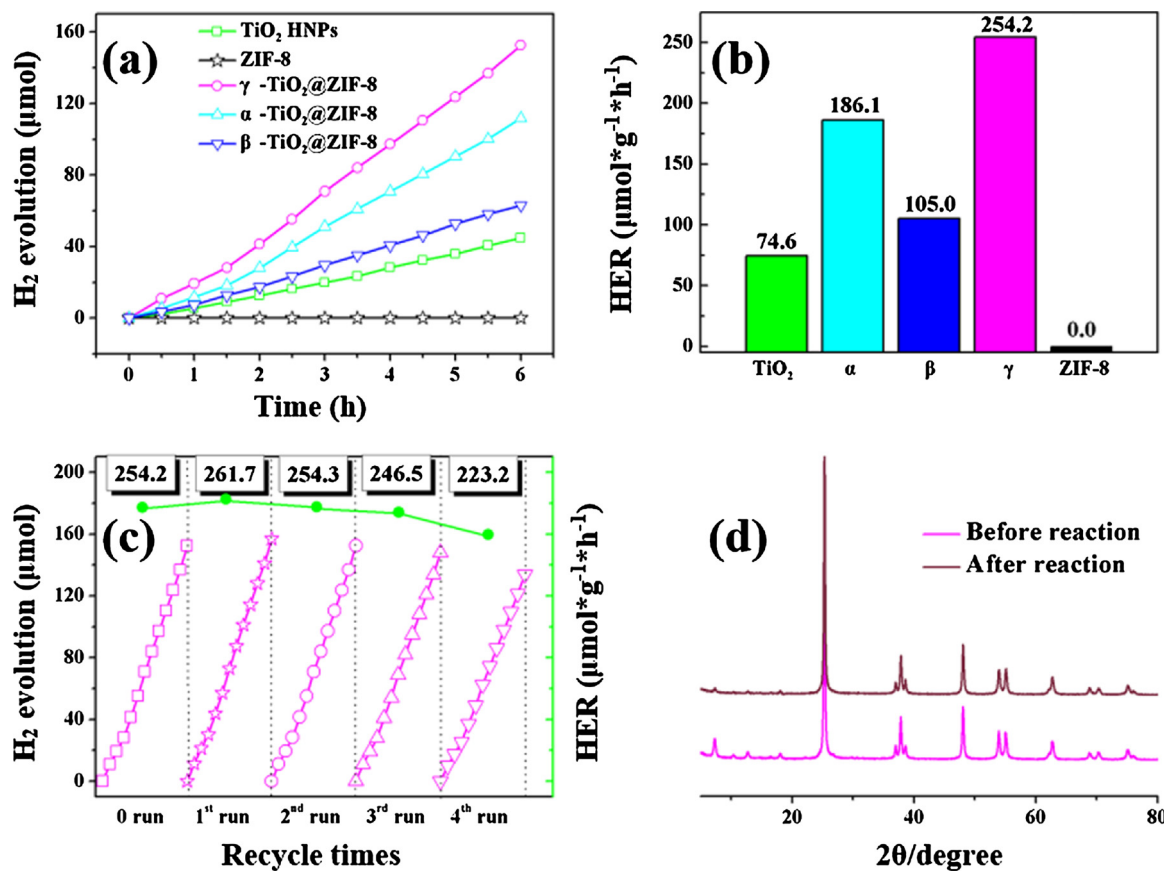


Fig. 11. (a) Photocatalytic hydrogen evolution performance of TiO₂ HNPs, ZIF-8 and α -/ β -/ γ -TiO₂@ZIF-8; (b) H₂ evolution rates; (c) Recyclability of H₂ evolution behavior of γ -TiO₂@ZIF-8; (d) PXRD patterns of γ -TiO₂@ZIF-8 before and after recycling 4 times.

the surface of TiO₂ HNPs, as presented, the γ -TiO₂@ZIF-8 exhibited the most obvious enhancement with 152.54 μmol of H₂ evolution (HER: 254.2 μmol g⁻¹ h⁻¹), which was about 3.4 times higher than that of bare TiO₂ HNPs. And α -/ β -TiO₂@ZIF-8 can elevated the HER to 186.1 μmol g⁻¹ h⁻¹ and 105.0 μmol g⁻¹ h⁻¹, respectively. In addition, there would be no photocatalytic enhancement if three TiO₂@ZIF-8 composites had no interaction between TiO₂ HNPs and ZIF-8 according to the nil HER of bare ZIF-8. Generally, it was accepted that the catalyst with a larger specific surface area showed higher photocatalytic performance. The smallest size and best coverage of ZIF-8 in TiO₂@ZIF-8 was from γ -TiO₂@ZIF-8, which could provide more active sites in photocatalytic reaction. Although the direct comparison of different photocatalysts for HER is not easy due to different experiment conditions, the AQE value of photocatalysts could reflect the ability of HER, Table S1 listed the hydrogen evolution behavior of related photocatalysts reported in recent years. The hybrid photocatalyst γ -TiO₂@ZIF-8 showed a 50.89% of apparent quantum efficiency (AQE) at 380 nm with excellent photocatalytic hydrogen evolution reaction activity and high efficiency for solar energy utilization.

The stability of photocatalytic hydrogen evolution of γ -TiO₂@ZIF-8 was also evaluated by reusing it for multiple hydrogen evolution reaction cycles. Five consecutive photocatalytic reactions were performed under artificial solar light irritation. As shown in Fig. 11c, the amount of generated H₂ increased steadily with the irradiation time in each cycle. Then it remained highly stable during a long-time test (30 h), and the HER value in the fifth recycle remained nearly the same as those in the first cycle, demonstrating the exceptional photocatalytic stability of γ -TiO₂@ZIF-8. Moreover, the XRD patterns (Fig. 11d) of γ -TiO₂@ZIF-8 before and after cycling in H₂ evolution experiments in the fifth showed a slight decrease of peaks intensity assignable to ZIF-8, indicating that there might be a small-scale dissolution of ZIF-8 part during the whole 5

runs in photocatalytic processing, which has been verified by the TG and BET measurement (Figs. S6 and S7).

To further know the reason for the enhanced photocatalytic activity of TiO₂@ZIF-8 for H₂ evolution as compared to bare TiO₂ HNPs and bare ZIF-8, steady-state photoluminescence (PL) and time-resolved transient photoluminescence decay spectra were carried out to investigate the formation and migration behavior of photogenerated charge carriers in prepared hybrid photocatalysts (Fig. 12). The PL emission of α -/ β -/ γ -TiO₂@ZIF-8 composites were remarkably lifted (Fig. 12a), revealing that the introduction of ZIF-8, containing an organic imidazole ring easily to be excited by MLCT mode, would added one more radiation pattern. In view of the possibility of the signal coverage by ZIF-8 self-excited, just an initial conclusion in experiments was made that the order of suppression of charge recombination from strong to weak was $\alpha > \gamma > \beta$. And then, further get the truth of the charge recombination, the time-resolved photoluminescence (TRPL) spectrum decay curves (Fig. 12b) were fitted by exponential decay kinetics function: $I(t) = A_1 \exp(-t/\tau_1) + A_2 \exp(-t/\tau_2)$, where τ_1 and τ_2 were the emission lifetimes, and A_1 and A_2 were the corresponding amplitudes. The τ_1 value was from the main body of TiO₂ in TiO₂@ZIF-8, which is the one of the luminescent species, while τ_2 value was an important indicator of the efficiency of the charge transfer and energy transfer [71,72]. As listed in Table S2, the τ_2 values of α -/ β -/ γ -TiO₂@ZIF-8 were 5.2686 ns, 6.6635 ns and 2.8344 ns, respectively. The lower lifetime of γ -TiO₂@ZIF-8 indicated that there were fewer radiative pathways from recombination of electron-hole pairs.

To better clarify the charge transfer property of the hybrid TiO₂@ZIF-8 composites on the photocatalytic activities, it was necessary to understand the intrinsic electronic properties and photoelectronic properties. The electrochemical impedance spectroscopy (EIS) could illustrate the separation of photogenerated electron-hole pairs and

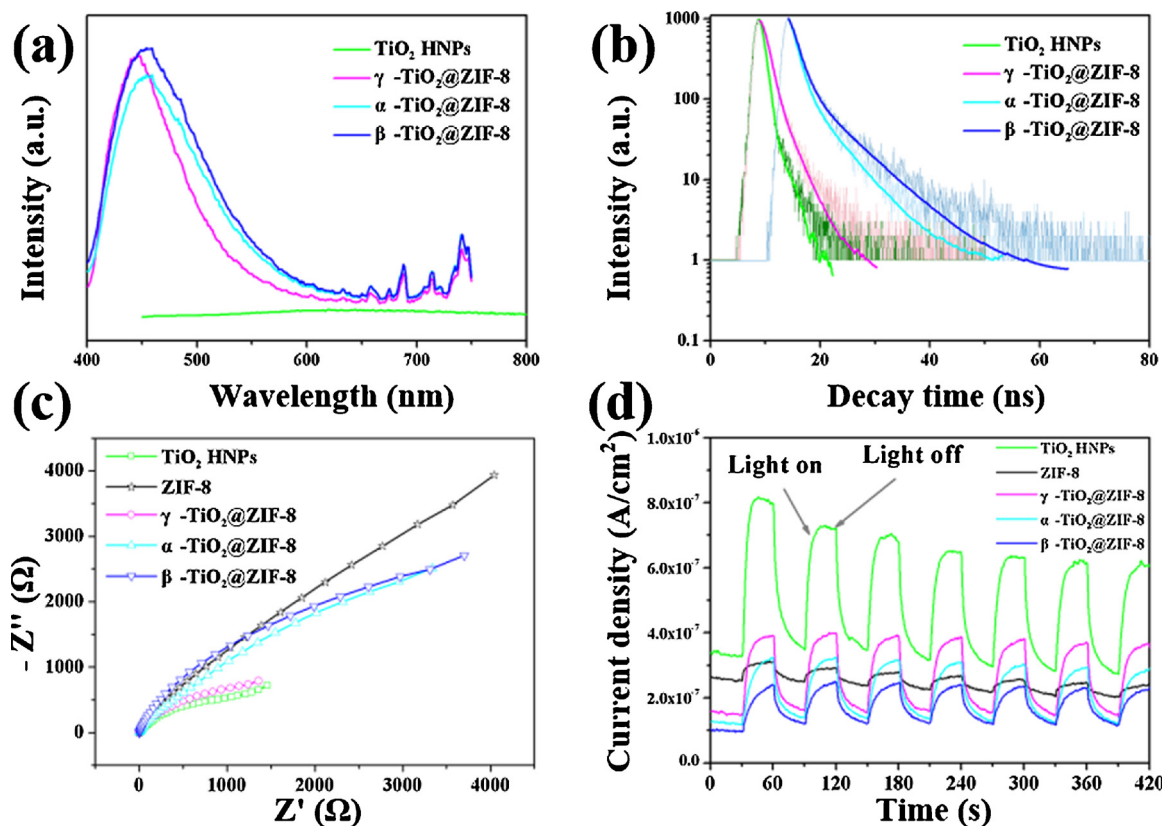


Fig. 12. (a) Photoluminescence of TiO₂ HNPs, and α -/ β -/ γ -TiO₂@ZIF-8; (b) Time-resolved photoluminescence decay transient of TiO₂ HNPs, and α -/ β -/ γ -TiO₂@ZIF-8; (c) Electrochemical impedance spectra of TiO₂ HNPs, ZIF-8 and α -/ β -/ γ -TiO₂@ZIF-8; (d) Photocurrent response of TiO₂ HNPs, ZIF-8 and α -/ β -/ γ -TiO₂@ZIF-8.

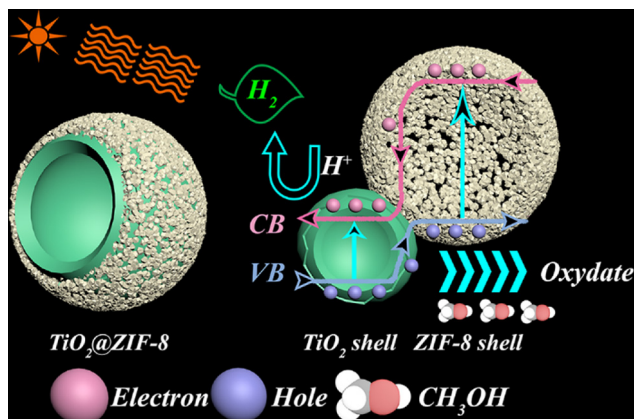


Fig. 13. Illustration of the HER mechanism over TiO₂@ZIF-8 under artificial solar light irradiation.

interfacial charge transfer resistance. Stimulated by charge migration, the EIS Nyquist plot would present an arc shape in the measurement results. A smaller arc radius on the plot suggested the superior charge transfer capability, which further facilitate the separation of photo-generated electron-hole pairs. As shown in Fig. 12c, the arc radius of bare TiO₂ HNPs and γ -TiO₂@ZIF-8 are smaller than that of α -/ β -TiO₂@ZIF-8 and bare ZIF-8. This result revealed that the ultrasonic synthesis could reach a more efficient promotion for charge transfer. Meanwhile, the i-t curves in Fig. 12d showed the fast photoelectronic responses that could demonstrate the separation and migration of photoinduced electrons and holes.

The photocurrent response of bare ZIF-8 was the weakest one. Although the TiO₂ HNPs showed the highest photocurrent density, its intensity would gradually fade for a successive long-time exposure to

sun light, which might be caused by the serious light corrosion without any protection in the surface of TiO₂ HNPs. While γ -TiO₂@ZIF-8 not only showed the highest photocurrent density in three hybrid TiO₂@ZIF-8 composites, but also can avoid the decay of photocurrent density for seven runs under solar light, indicating the good reversibility and stability of the photoanode. This enhanced transient photocurrent density could be attributed to the suppression of electron-hole recombination realized by the coating of ZIF-8 via sonocrystallization.

The photocatalytic HER mechanism was proposed in Fig. 13. The schematic illustration of separation of photoinduced electron-hole pairs in hybrid TiO₂@ZIF-8 composites was present. The band gap of TiO₂@ZIF-8 was about 3.28 eV, and the valence band (VB) and conduction band (CB) energy levels were about 2.08 and -1.19 eV (vs. NHE), respectively. Compared with the -0.41 eV (vs. NHE) of $2H^+ / H_2$ reduction potential, the value of E_c of the photocatalyst was more negative, indicating its good photocatalytic H₂ evolution capability. Compared to bare TiO₂ with -0.31 eV of E_c value, TiO₂@ZIF-8 can result in enhanced photocatalytic efficiency due to the more negative conduction band edges [73,74]. Under solar light irritation, both TiO₂ HNPs and ZIF-8 could be excited by light and the electron transfer could be in two pathways. On the one hand, the electrons were excited to CB of TiO₂ HNPs from the VB resulting in reducing proton to H₂. On the other hand, the valence band electrons in ZIF-8 were excited to the CB of TiO₂ HNPs for H₂ evolution, while the sacrificial reagent (methanol) would complement the electrons to the remaining holes in the VB of ZIF-8 from TiO₂ HNPs. In turn, the cage structure of ZIF-8 with lots of active reaction sites can increase the contact area with substrate in solution over entire surface of catalytic support surface for H₂ generation. And the good photocatalytic capability investigated by the BET and photoelectronic measurements could enhance the surface reaction.

4. Conclusions

In summary, double-shell TiO₂@ZIF-8 hollow nanospheres were successfully synthesized via sonocrystallization in a certain charging sequence. The hybrid photocatalyst exhibited high hydrogen evolution rate up to 261.7 μmol g⁻¹ h⁻¹ under artificial solar light and high quantum efficiencies of 50.89% at 380 nm, representing the outstanding promoted catalytic activity. The composite heterostructures, for efficient charge separation with electron injection from ZIF-8 to TiO₂ HNPs, also maintained a high surface area for exposing more active sites in photocatalysis. Moreover, the excellent stability could be verified by a long-time test for 30 h. This study, demonstrating that photocatalytic H₂ evolution over TiO₂ can be improved with the use of ZIF-8 as charge separator and active-sites supplier, highlighted the great potential of MOF-based semiconductor composite materials for solar-light-driven photocatalysis.

Acknowledgements

This work was supported by the National Natural Science Foundation of China (21301131 and 21477118), the Natural Science Foundation of Hubei Province (2013CFB313) and the open fund of Engineering Research Center of Nano-Geo Materials of Ministry of Education, China University of Geosciences (Wuhan) (NGM2016KF013).

Appendix A. Supplementary data

Supplementary material related to this article can be found, in the online version, at doi: <https://doi.org/10.1016/j.apcatb.2018.09.036>.

References

- [1] R. Liu, X.Z. Sun, X.X. Song, Y.Z. Zhang, L. Xu, L. Xi, *Appl. Catal. A: Gen.* 544 (2017) 137–144.
- [2] D. Ma, J.W. Shi, Y. Zou, Z. Fan, X. Ji, C. Niu, *ACS Appl. Mater. Interfaces* 9 (2017) 25377–25386.
- [3] S. Al-Meer, Z.K. Ghouri, K. Elsaied, A. Easa, M.T. Al-Qahtani, M.S. Akhtar, *J. Alloys Compd.* 723 (2017) 477–483.
- [4] H. Imahori, S. Kang, H. Hayashi, M. Haruta, H. Kurata, S. Isoda, S.E. Canton, Y. Infahsaeng, A. Kathiravan, T. Pascher, P. Chabera, A.P. Yartsev, V. Sundstrom, *J. Phys. Chem. A* 115 (2011) 3679–3690.
- [5] S. Cao, J. Yu, *J. Phys. Chem. Lett.* 5 (2014) 2101–2107.
- [6] S. Zhang, H. Yang, H. Gao, R. Cao, J. Huang, X. Xu, *ACS Appl. Mater. Interfaces* 9 (2017) 23635–23646.
- [7] R. Long, Y. Li, Y. Liu, S. Chen, X. Zheng, C. Gao, C. He, N. Chen, Z. Qi, L. Song, J. Jiang, J. Zhu, Y. Xiong, *J. Am. Chem. Soc.* 139 (2017) 4486–4492.
- [8] O.K. Varghese, M. Paulose, T.J. LaTempa, C.A. Grimes, *Nano Lett.* 9 (2009) 731–737.
- [9] Y. Tachibana, L. Vayssières, J.R. Durrant, *Nat. Photonics* 6 (2012) 511–518.
- [10] P.D. Tran, L.H. Wong, J. Barber, J.S.C. Loo, *Energy Environ. Sci.* 5 (2012) 5902–5918.
- [11] Q. Xiang, J. Yu, M. Jaroniec, *Chem. Soc. Rev.* 41 (2012) 782–796.
- [12] A. Fujishima, K. Honda, *Nature* 238 (1972) 37–38.
- [13] S.N. Frank, A.J. Bard, *J. Phys. Chem.* 81 (1977) 1484–1488.
- [14] M.R. Hoffmann, S.T. Martin, W.Y. Choi, D.W. Bahnemann, *Chem. Rev.* 95 (1995) 69–96.
- [15] T.L. Thompson, J.T. Yates Jr., *Chem. Rev.* 106 (2006) 4428–4453.
- [16] A. Mills, S. LeHunte, *J. Photoch. Photobio. A* 108 (1997) 1–35.
- [17] C.W. Raubach, Y.V.B. De Santana, M.M. Ferrer, P.G.C. Buzolin, J.R. Sambrano, E. Longo, *Dalton Trans.* 42 (2013) 11111–11116.
- [18] M.D. Hernandez-Alonso, F. Fresno, S. Suarez, J.M. Coronado, *Energy Environ. Sci.* 2 (2009) 1231–1257.
- [19] S.J. Yang, J.H. Im, T. Kim, K. Lee, C.R. Park, *J. Hazard. Mater.* 186 (2011) 376–382.
- [20] Z. Genqiang, W.H. Bin, S. Taeseup, P. Ungyu, L.X. Wen, *Angew. Chem.* 126 (2014) 12798–12801.
- [21] S. Kobayashi, K. Hanabusa, N. Hamasaki, M. Kimura, H. Shirai, S. Shinkai, *Chem. Mater.* 12 (2000) 1523–1525.
- [22] J.S. Chen, Y.L. Tan, C.M. Li, Y.L. Cheah, D. Luan, S. Madhavi, F.Y.C. Boey, L.A. Archer, X.W. Lou, *J. Am. Chem. Soc.* 132 (2010) 6124–6130.
- [23] R. Asahi, T. Morikawa, T. Ohwaki, K. Aoki, Y. Taga, *Science* 293 (2001) 269–271.
- [24] Q. Xiang, J. Yu, W. Wang, M. Jaroniec, *Chem. Commun.* 47 (2011) 6906–6908.
- [25] Q. Xiang, J. Yu, M. Jaroniec, *J. Am. Chem. Soc.* 134 (2012) 6575–6578.
- [26] A. Fujishima, X. Zhang, D.A. Tryk, *Surf. Sci. Rep.* 63 (2008) 515–582.
- [27] X. Chen, S. Shen, L. Guo, S.S. Mao, *Chem. Rev.* 110 (2010) 6503–6570.
- [28] K.S. Park, Z. Ni, A.P. Cote, J.Y. Choi, R. Huang, F.J. Uribe-Romo, H.K. Chae, M. O’Keeffe, O.M. Yaghi, *Proc. Natl. Acad. Sci. U. S. A.* 103 (2006) 10186–10191.
- [29] M. Alvaro, E. Carbonell, B. Ferrer, F.X. Llabres i Xamena, H. Garcia, *Chem. A Eur. J.* 13 (2007) 5106–5112.
- [30] M. Fuentes-Cabrera, D.M. Nicholson, B.G. Sumpter, M. Widom, *J. Chem. Phys.* 123 (2005) 124713–124716.
- [31] K.G.M. Laurier, F. Verwoortele, R. Ameloot, D.E. De Vos, J. Hofkens, M.B.J. Roefers, *J. Am. Chem. Soc.* 135 (2013) 14488–14491.
- [32] Z.T. Yu, Z.L. Liao, Y.S. Jiang, G.H. Li, J.S. Chen, *Chem. A Eur. J.* 11 (2005) 2642–2650.
- [33] Y. Lee, S. Kim, H. Fei, J.K. Kang, S.M. Cohen, *Chem. Commun.* 51 (2015) 16549–16552.
- [34] T. Zhou, Y. Du, A. Borgna, J. Hong, Y. Wang, J. Han, W. Zhang, R. Xu, *Energy Environ. Sci.* 6 (2013) 3229–3234.
- [35] Y. Chen, J. Li, G. Yue, X. Luo, *Nano-Micro Lett.* 9 (2017) 32–42.
- [36] Y. Zhao, Y. Dong, F. Lu, C. Ju, L. Liu, J. Zhang, B. Zhang, Y. Feng, *J. Mater. Chem. A* 5 (2017) 15380–15389.
- [37] S. Yan, S. Ouyang, H. Xu, M. Zhao, X. Zhang, J. Ye, *J. Mater. Chem. A* 4 (2016) 15126–15133.
- [38] A. Crake, K.C. Christoforidis, A. Kafizas, S. Zafeiratos, C. Petit, *Appl. Catal. B: Environ.* 210 (2017) 131–140.
- [39] H. Sheng, D. Chen, N. Li, Q. Xu, H. Li, J. He, J. Lu, *Chem. Mater.* 29 (2017) 5612–5616.
- [40] L.T.L. Nguyen, K.K.A. Le, N.T.S. Phan, *Chin. J. Catal.* 33 (2012) 688–696.
- [41] U.P.N. Tran, K.K.A. Le, N.T.S. Phan, *ACS Catal.* 1 (2011) 120–1271.
- [42] H.P. Jing, C.C. Wang, Y.W. Zhang, P. Wang, R. Li, *RSC Adv.* 4 (2014) 54454–54462.
- [43] B. Yu, F. Wang, W. Dong, J. Hou, P. Lu, J. Gong, *Mater. Lett.* 156 (2015) 50–53.
- [44] X. Wang, J. Liu, S. Leong, X. Lin, J. Wei, B. Kong, Y. Xu, Z.-X. Low, J. Yao, H. Wang, *ACS Appl. Mater. Interfaces* 8 (2016) 9080–9087.
- [45] Q. Liu, Z.-X. Low, L. Li, A. Razmjou, K. Wang, J. Yao, H. Wang, *J. Mater. Chem. A* 1 (2013) 11563–11569.
- [46] X. Zeng, L. Huang, C. Wang, J. Wang, J. Li, X. Luo, *ACS Appl. Mater. Interfaces* 8 (2016) 20274–20282.
- [47] K.S. Suslick, S.B. Choe, A.A. Cichowlas, M.W. Grinstaff, *Nature* 353 (1991) 414–416.
- [48] N. Zhang, C. Han, Y.-J. Xu, J.J. Foley, D. Zhang, J. Codrington, S.K. Gray, Y. Sun, *Nat. Photonics* 10 (2016) 473–482.
- [49] Y. Wei, G. Cheng, J. Xiong, F. Xu, R. Chen, *ACS Sustain. Chem. Eng.* 5 (2017) 5027–5038.
- [50] D. Saliba, M. Ammar, M. Rammal, M. Al-Ghoul, M. Hmadeh, *J. Am. Chem. Soc.* 140 (2018) 1812–1823.
- [51] L.H. Wee, N. Janssens, S.P. Sree, C. Wiktor, E. Gobechiya, R.A. Fischer, C.E.A. Kirschhoek, J.A. Martens, *Nanoscale* 6 (2014) 2056–2060.
- [52] Y. Hu, H. Kazemian, S. Rohani, Y. Huang, Y. Song, *Chem. Commun.* 47 (2011) 12694–12696.
- [53] J. Yao, R. Chen, K. Wang, H. Wang, *Microporous Mesoporous Mater.* 165 (2013) 200–204.
- [54] S.D. Perera, R.G. Mariano, V. Khiem, N. Nour, O. Seitz, Y. Chabal, K.J. Balkus Jr., *ACS Catal.* 2 (2012) 949–956.
- [55] S. Schlueter, *Angew. Chem. Int. Ed.* 53 (2014) 4756–4795.
- [56] J.C. Parker, R.W. Siegel, *Appl. Phys. Lett.* 57 (1990) 943–945.
- [57] M. Anpo, M. Che, B. Fubini, E. Garrone, E. Giannello, M.C. Paganini, *Top. Catal.* 8 (1999) 189–198.
- [58] L. Schlur, S. Begin-Colin, P. Gilliot, M. Gallart, G. Carré, S. Zafeiratos, N. Keller, V. Keller, P. André, J.-M. Grenache, B. Hezard, M.H. Desmonts, G. Pourroy, *Mater. Sci. Eng. C* 38 (2014) 11–19.
- [59] N. Shi, X. Li, T. Fan, H. Zhou, J. Ding, D. Zhang, H. Zhu, *Energy Environ. Sci.* 4 (2011) 172–180.
- [60] V. Papaeftimiou, T. Dintzer, M. Lebedeva, D. Teschner, M. Hävecker, A. Knop-Gericke, R. Schlögl, V. Pierron-Bohnes, E. Savinova, S. Zafeiratos, *J. Phys. Chem. C* 116 (2012) 14342–14349.
- [61] F. Tian, A.M. Cerro, A.M. Mosier, H.K. Wayment-Steele, R.S. Shine, A. Park, E.R. Webster, L.E. Johnson, M.S. Johal, L. Benz, *J. Phys. Chem. C* 118 (2014) 14449–14456.
- [62] Y. Deng, L. Tang, G. Zeng, Z. Zhu, M. Yan, Y. Zhou, J. Wang, Y. Liu, J. Wang, *Appl. Catal. B: Environ.* 203 (2017) 343–354.
- [63] H. Wang, X. Yuan, Y. Wu, G. Zeng, X. Chen, L. Leng, Z. Wu, L. Jiang, H. Li, J. Hazard. Mater. 286 (2015) 187–194.
- [64] Z. Yan, H. Yang, J. Ouyang, A. Tang, *Chem. Eng. J.* 316 (2017) 1035–1046.
- [65] J. Liu, R. Han, Y. Zhao, H. Wang, W. Lu, T. Yu, Y. Zhang, *J. Phys. Chem. C* 115 (2011) 4507–4515.
- [66] H. Pi, D. Zhang, X. Zhang, Z. Jin, L. Zhang, X. Cui, W. Zheng, *Dalton Trans.* 47 (2018) 209–214.
- [67] X. Yang, Z. Wen, Z. Wu, X. Luo, *Inorg. Chem. Front.* 5 (2018) 687–693.
- [68] X. Yu, W. Li, Z. Li, J. Liu, P. Hu, *Appl. Catal. B: Environ.* 217 (2017) 48–56.
- [69] A. Nayak, P.S. Rama Sreekanth, S.K. Sahu, D. Sahu, *Chin. J. Polym. Sci.* 35 (2017) 1073–1085.
- [70] G. Liu, P. Niu, L. Yin, H.M. Cheng, *J. Am. Chem. Soc.* 134 (2012) 9070–9073.
- [71] T. Jia, A. Kolpin, C. Ma, R.C.T. Chan, W.-M. Kwok, S.C.E. Tsang, *Chem. Commun.* 50 (2014) 1185–1188.
- [72] M.Y. Ye, Z.H. Zhao, Z.F. Hu, L.Q. Liu, H.M. Ji, Z.R. Shen, T.Y. Ma, *Angew. Chem. Int. Ed.* 56 (2017) 8407–8411.
- [73] M. Wen, K. Mori, Y. Kuwahara, T. An, H. Yamashita, *Chem.-Asian J.* 13 (2018) 1767–1779.
- [74] M. Wen, K. Mori, Y. Kuwahara, T. An, H. Yamashita, *Appl. Catal. B: Environ.* 218 (2017) 555–569.